Article

Molecular rearrangement of bicyclic peroxy radicals is a key route to aerosol from aromatics

Check for updates

Siddharth Iyer [1] ✉, Avinash Kumar [1], Anni Savolainen [1], Shawon Barua [1], Christopher Daub [2], Lukas Pichelstorfer[3], Pontus Roldin [4,5], Olga Garmash[1,6], Prasenjit Seal[1], Theo Kurtén [2] & Matti Rissanen [1,2] ✉

The oxidation of aromatics contributes significantly to the formation of atmospheric aerosol. Using toluene as an example, we demonstrate the existence of a molecular rearrangement channel in the oxidation mechanism. Based on both flow reactor experiments and quantum chemical calculations, we show that the bicyclic peroxy radicals (BPRs) formed in OH-initiated aromatic oxidation are much less stable than previously thought, and in the case of the toluene derived ipso-BPRs, lead to aerosol-forming low-volatility products with up to 9 oxygen atoms on sub-second timescales. Similar results are predicted for ipso-BPRs formed from many other aromatic compounds. This reaction class is likely a key route for atmospheric aerosol formation, and including the molecular rearrangement of BPRs may be vital for accurate chemical modeling of the atmosphere.

Aromatic hydrocarbons are an important class of atmospheric trace gases. The global emissions of the most important aromatic molecules, benzene, toluene, ethylbenzene and xylenes (collectively known as BTEX), account for 23% of the global anthropogenic non-methane hydrocarbons on a per-carbon basis[1] and up to 60% of the urban emissions[2,3]. Their sources are primarily anthropogenic, such as from incomplete combustion, industrial processes, and solvent evaporation[4-9]. Recent studies have shown that biogenic sources of BTEX, such as from terrestrial vegetation and from marine phytoplanktons, are also important[10-12], and they have even been measured in the remote Southern ocean and in the arctic[13,14]. Aromatic hydrocarbons in the gas phase pose serious health risks directly[15-18] and also indirectly as their secondary chemistry can lead to tropospheric ozone and secondary organic aerosol (SOA) production[19-23]. The latter can have implications on the planet's radiative balance by affecting the formation and properties of clouds, but significant uncertainties remain regarding the extent of these radiative effects[24-26].

In order to form SOA, participating vapors need to have sufficiently low volatility, which in practice implies molecules with multiple oxygen-containing polar functional groups. Autoxidation[27] has been shown to efficiently form SOA from various aliphatic VOCs, and the molecular level mechanism has been fairly well established for a few key aliphatics[28-31]. Laboratory studies show that aromatics also autoxidize and form SOA efficiently[22], but all presented molecular level aromatic oxidation mechanisms are far too slow to explain observations. This is a problem because the accurate modeling of SOA from aromatics requires accurately predicting the paths that lead to SOA.

The oxidative chemistry of aromatic hydrocarbons is mainly initiated by OH radicals. In a majority of cases, the reaction of OH with BTEX molecules involves addition to the aromatic ring, with H-atom abstraction playing a minor role at atmospherically relevant temperatures[32]. For toluene, OH addition to the ortho position accounts for 69.8%, followed by ipso, para and meta additions (7.3%, 5.1%, 5.1%, respectively)[33]. The addition reaction leads to the formation of the bridged bicyclic peroxy radical (BPR[34]) as a major product. The

[1]Aerosol Physics Laboratory, Tampere University, FI-33101 Tampere, Finland. [2]Department of Chemistry, University of Helsinki, P.O. Box 55, FI-00014 Helsinki, Finland. [3]Pi-Numerics, 5202 Neumarkt am Wallersee, Austria. [4]Department of Physics, Lund University, P.O. Box 118, SE-221 00 Lund, Sweden. [5]Swedish Environmental Research Institute IVL, SE-211 19 Malmö, Sweden. [6]Department of Atmospheric Sciences, University of Washington, Seattle, WA, USA. ✉e-mail: siddharth.iyer@tuni.fi; matti.rissanen@tuni.fi

critical early steps of toluene oxidation by OH addition are described in Supplementary Section 2. The formation of the BPR from toluene oxidation is considered to be a mechanistic branching point as it has so far been thought to require bimolecular reaction partners to further oxidize due to slow unimolecular reaction rate coefficients ($< 0.03\,s^{-1}$[35]). This is due to the double-ringed structure that sterically hinders both intramolecular H-shift and ring closure reactions forming endoperoxides. In contrast to this mechanistic understanding, flow reactor measurements at 7.9 s reaction time show that the initially formed BPR will quickly add several more oxygen atoms to form peroxy radicals with up to 9 oxygen atoms[35]. These discrepancies suggest an alternative unimolecular fate of the BPR that is both rapid and completely neglected in previous studies.

In this work, we conclusively demonstrate that the toluene derived ipso BPR (i-BPR) is unstable under atmospheric conditions, and undergoes spontaneous molecular rearrangement. This reaction leads to completely ring broken RO_2s, a prerequisite for efficient autoxidation, at rates competitive with bimolecular reactions with NO even under polluted conditions. Intriguingly, several of the organo nitrates and other closed shell products derived from the i-BPR are likewise unstable and decompose on regional atmospheric transport timescales. This could provide, e.g., a transport reservoir for NO_x similar to peroxyacyl nitrates (PAN). Using quantum chemical calculations and master equation simulations that account for energy non-accommodation, we elucidate the molecular level mechanism of the subsequent autoxidation of the ring broken RO_2s that leads rapidly to the highly oxygenated SOA precursor molecules with up to nine oxygen atoms in sub-second timescales. Furthermore, using targeted flow reactor experiments of the OH reaction of toluene and partially deuterated toluene with nitrate chemical ionization mass spectrometry (NO_3-CIMS) detection, we corroborate the proposed mechanism. This is the only unambiguous reaction pathway to toluene derived SOA precursors reported to date.

Results and discussion
Spontaneous molecular rearrangement of i-BPR

The rearrangement of i-BPR occurs by the concomitant cleavage of a C-C bond and the O-O bond, along with an H-shift (see Fig. 1a) to lead to a completely ring broken RO_2 with two carbonyl (=O) groups and one hydroxyl (−OH) group. Two rearrangement pathways are possible, C_1 and C_2, depending on which of the two C-C bonds are broken. Relative to the i-BPR, the energy barriers for C_1 and C_2 are 18.8 kcal/mol and 17.9 kcal/mol, respectively, and the energies of the ring broken RO_2s, P-C_1 and P-C_2, are −51.7 kcal/mol and −49.4 kcal/mol, respectively. All energies reported here are zero-point corrected energies. At $P = 1$ atm and $T = 300$ K, the unimolecular rate coefficients of the two pathways are $0.16\,s^{-1}$ and $0.59\,s^{-1}$, respectively, which are competitive with RO_2 bimolecular reactions with NO even under heavily polluted conditions. The predicted rate coefficients as a function of temperature are shown in Fig. 1b. Toluene derived BPRs with OH in the ortho, meta and para positions can also undergo the two rearrangement mechanisms, but they are significantly slower and follow the trend of ipso>meta>para>ortho. The rearrangement rate coefficients for meta, para and ortho BPRs are provided in Supplementary Table 7. In addition to being an order-of-magnitude faster than any previously reported isomerization reaction of a toluene derived BPR, the significant exothermicity of the formation of the products means that the rearrangement reactions are irreversible. This is important since some of those previously reported isomerization reactions of BPR, specifically H-shift reactions, were reversible with reverse rate coefficients that are competitive with the bimolecular recombination reactions with O_2 under atmospheric conditions[35].
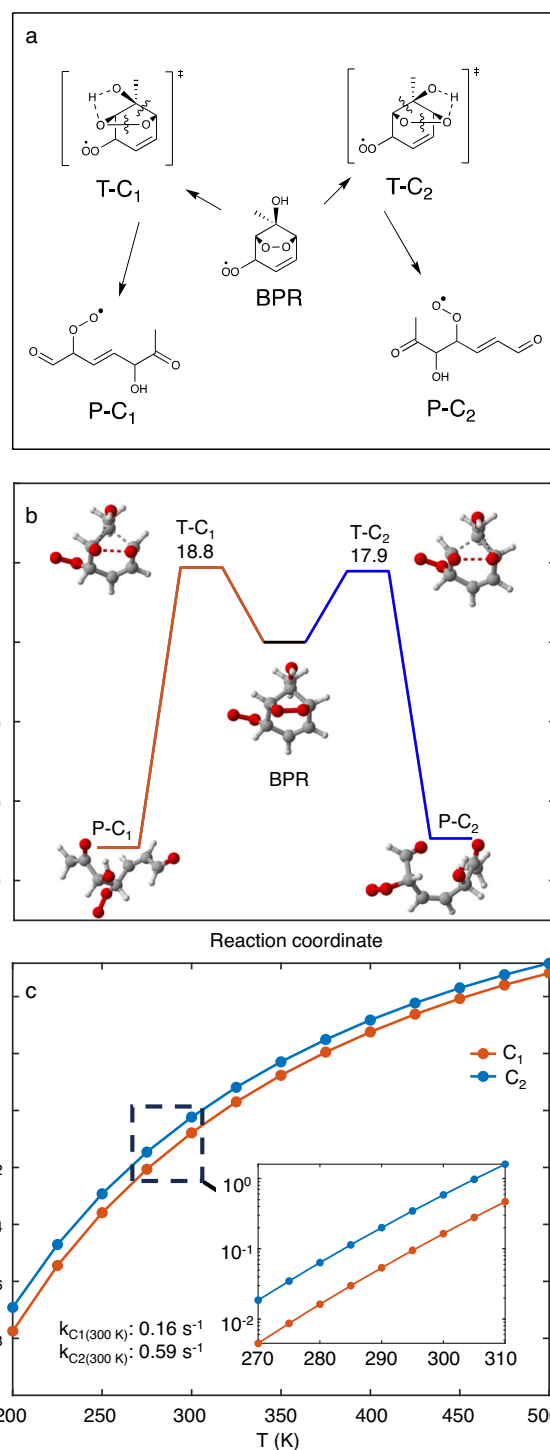

Fig. 1 | Molecular rearrangement mechanisms of i-BPR. a 2-D schematic of the two ring breaking mechanisms C_1 and C_2. **b** Stationary points along the potential energy surface of the ring breaking mechanisms with zero-point corrected energies on the y-axis and the reaction coordinate on the x-axis. **c** Master equation derived rate coefficients of the ring breaking mechanisms C_1 and C_2 as a function of temperature (at $P = 1$ atm). Additional points in the atmospherically relevant temperature range are provided in the inset. BPR = bicyclic peroxy radical, T-$C_{1,2}$ = transition states for ring opening pathways 1,2; P-$C_{1,2}$ = corresponding ring broken products. Color coding of atoms: gray - carbon, red oxygen, white - hydrogen.

Subsequent autoxidation of ring broken peroxy radicals from i-BPR

Both molecular rearrangement mechanisms of i-BPR are expected to occur, leading to the two ring broken RO_2s from i-BPR, $P-C_1$ and $P-C_2$. These will subsequently autoxidize rapidly in the absence of the steric hindrance of structural rings, as we have shown previously for the α-pinene ozonolysis system[28]. Master equation simulations also show that the excess energy carried by $P-C_1$ and $P-C_2$ allows them to access multiple autoxidation pathways simultaneously. Figure 2 shows the master equation simulation derived initial yields of $P-C_1$ and $P-C_2$, and the yields of the three intermediates formed from the lowest energy barrier autoxidation pathways of $P-C_2$: R_1, R_2 and R_3. The corresponding intermediates from $P-C_1$ were also included in the master equation simulation, but are excluded in Fig. 2. The three autoxidation pathways of $P-C_2$ are shown with differently colored arrows for clarity. Green is the dominant pathway (59%) because the 1,6 H-shift leading to the alkyl radical R_1 has the lowest energy barrier. R_1 can either react with O_2 to lose HO_2 and form the carbonyl compound $C_7H_8O_5$, or add an O_2 to form the peroxy radical $R_{1b}-RO_2$. $R_{1b}-RO_2$ will isomerize via a 1,6 H-shift to form the $R_{1b}-OOH$-vinoxy radical, that subsequently adds an O_2 to form the O_9-RO_2 $C_7H_9O_9$. The branching between the carbonyl and peroxy radical pathways is estimated in Supplementary Section 8. The pathway indicated by blue arrows has the next highest yield (16%), and can lead to the $O_{11}-RO_2$ $C_7H_9O_{11}$. Finally, the pathway with red arrows has the lowest initial yield, but can subsequently isomerize rapidly to form the O_7-RO_2 $C_7H_9O_7$ (R_3-Epo-RO_2), followed by a 1,5 H-shift with a relatively slower rate coefficient to form the O_9-RO_2 (R_3-Epo-OOH-$R"O_2$). R_3 and R_3-Epo-R' both have small reverse barriers, but the yield of R_3-Epo-RO_2 is nevertheless likely to be high due to the excess energy of $P-C_2$ as shown in our simulations (see Supplementary Section 12). Note that the last radical intermediates shown for each of the three pathways can continue to autoxidize to form even higher oxygenated products. Due to difficulties in accurately treating the transition states of H-shift reactions from hydroxy groups computationally (see Methods and ref. [31]), the yield of R_3 was calculated at a lower level of theory. Therefore, the final yields of R_1, R_2 and R_3 shown in Fig. 2 likely have high uncertainties.

Experimental results

NO_3-CIMS coupled to a flow reactor was used to explore the formation of the oxidized products from the reaction of OH with toluene and the partially deuterated CD_3-toluene, where the methyl H-atoms are substituted with D-atoms. Experiments carried out at the short residence times (RT) of 0.8–3.7 s, show that $C_7H_9O_9$ (O_9-RO_2) with the nominal mass-to-charge ratio of 299 Th is rapidly formed. It is the dominant product peak already at 1.5 s RT, likely due to a combination of two factors: 1) its accumulation at short residence times and 2) the higher sensitivity of the NO_3-CIMS for the higher oxygenated products[36]. The recorded spectra and product signals during the 0.8 and 1.5 s RT experiments are shown in Supplementary Figs. 1, 2, while Fig. 3 shows the same during the 3.7 s RT experiment. Even higher oxygenated $C_7H_9O_{11}$ RO_2 was also detected at this RT, albeit at much lower signal.

The rapid formation of O_9-RO_2 agrees with the proposed mechanism from our quantum chemical calculations. Identical results are observed for the partially deuterated CD_3-toluene system, which is in line with the proposed mechanism where the methyl group plays no role in the formation of the oxidized products. This is in disagreement with the previous mechanistic understanding where Wang et al. showed that the only unimolecular reaction that could potentially be competitive under atmospheric conditions is the H-abstraction from the methyl group for the toluene derived BPR with OH in the para position[35]. They also reported that the subsequent peroxy radical will quickly lose the abstracted methyl H-atom to OH loss with a rate coefficient of 8 s^{-1} at 298 K, forming a closed-shell carbonyl compound.

However, their computed rate coefficient of 0.026 s^{-1} for the H-abstraction would indicate that bimolecular reactions with NO is likely the dominant sink of the BPR. It is also not sufficiently fast to completely explain their measurement of the 9-oxygen containing RO_2 (O_9-RO_2) from toluene + OH at their 7.9 s experimental residence time. Nevertheless, if this is the dominant fate of the toluene + OH system in our experiments, it would compete with the mechanism proposed in this study. However, our CD_3-toluene experiments showed that the dominant closed-shell and peroxy radical products detected contained all three D atoms (see Supplementary Fig. 11), indicating that the mechanism proposed in this work is likely to be the dominant unimolecular pathway to the SOA precursors that we detect. Note that D-shift rates are slower than H-shift rates due to isotope effects, in particular lower tunneling factors, so the use of CD_3-toluene will to an extent underestimate the role of H-shift from the methyl group. However, we observe that the mass spectra for toluene and CD_3-toluene are near identical, indicating that H-shift from the methyl group is unlikely to play a major role in our experiments. Nevertheless, this pathway might well be important under certain atmospheric conditions. The methyl H-abstraction pathway reported in ref. [35] and the rearrangement pathway reported here do not compete with each other but depend on the site of the initial OH addition to toluene (para vs ipso relative to the methyl substituent). D_2O experiments revealed that the dominant peak corresponding to O_9-RO_2 contains only two exchangeable H-atoms. This is more consistent with the mechanism we propose because the formed O_9-RO_2 via the dominant green pathway in Fig. 2 has two groups with exchangeable H-atoms. Following the previously proposed mechanism, RO_2 with three exchangeable H-atoms should form, which is not the case. The blue pathway in Fig. 2 does lead to a O_9-RO_2 with three exchangeable H-atoms, but likely due to its fast isomerization reaction (~230 s^{-1}) rapidly forms O_{11}-RO_2, and is not measured. In addition, the D_2O experiments also indicated two isomers of the O_7-RO_2, with one and two D-atoms, respectively (see Supplementary Figs 14, 15). While the latter is expected in previous and in our mechanisms, the former can occur if the autoxidation follows the red pathway in Fig. 2 that leads to an O_7-RO_2 with one exchangeable H-atom. Note that autoxidation is known to produce many isomers and the pathways shown in Fig. 2 are not the only autoxidation pathways occurring in our measurements. However, these are the only pathways that can currently explain the observed H-to-D shifts in the isomers we measure. Details of the D_2O experiments are provided in Supplementary Section 5.

To confirm that these compounds are in fact peroxy radicals, NO was added to form the corresponding organo nitrate ($RONO_2$) products. These experiments clearly illustrated the occurrence of the expected organo nitrates (see Supplementary Figs 12, 13). Reactions of peroxy radicals with NO can also lead to alkoxy radicals and the molecule can continue to oxidize via the alkoxy-peroxy autoxidation pathway. However, the resulting peroxy radicals will have an even number of oxygen atoms and not odd as the peroxy radicals involved in the formation of the organo nitrates reported in this study. The peroxy radicals are unlikely to undergo two NO reactions to revert to an odd number of oxygen atoms followed by a third NO reaction to produce the organo nitrates we detect under the short residence time conditions of our experiments.

The evolution of the oxidation products in the flow tube measurements was also modeled using the Aerosol Dynamics gas- and particle-phase chemistry model for laboratory CHAMber (ADCHAM) studies[37]. This model couples the i-BPR rearrangement pathways described in this work with the conventional Master Chemical Mechanism chemistry of toluene, and achieves a reasonable agreement with the flow reactor data despite the usage of lumped rate coefficients and uncertain branching ratios for the different pathways in toluene oxidation. Details are provided in Supplementary Section 9.
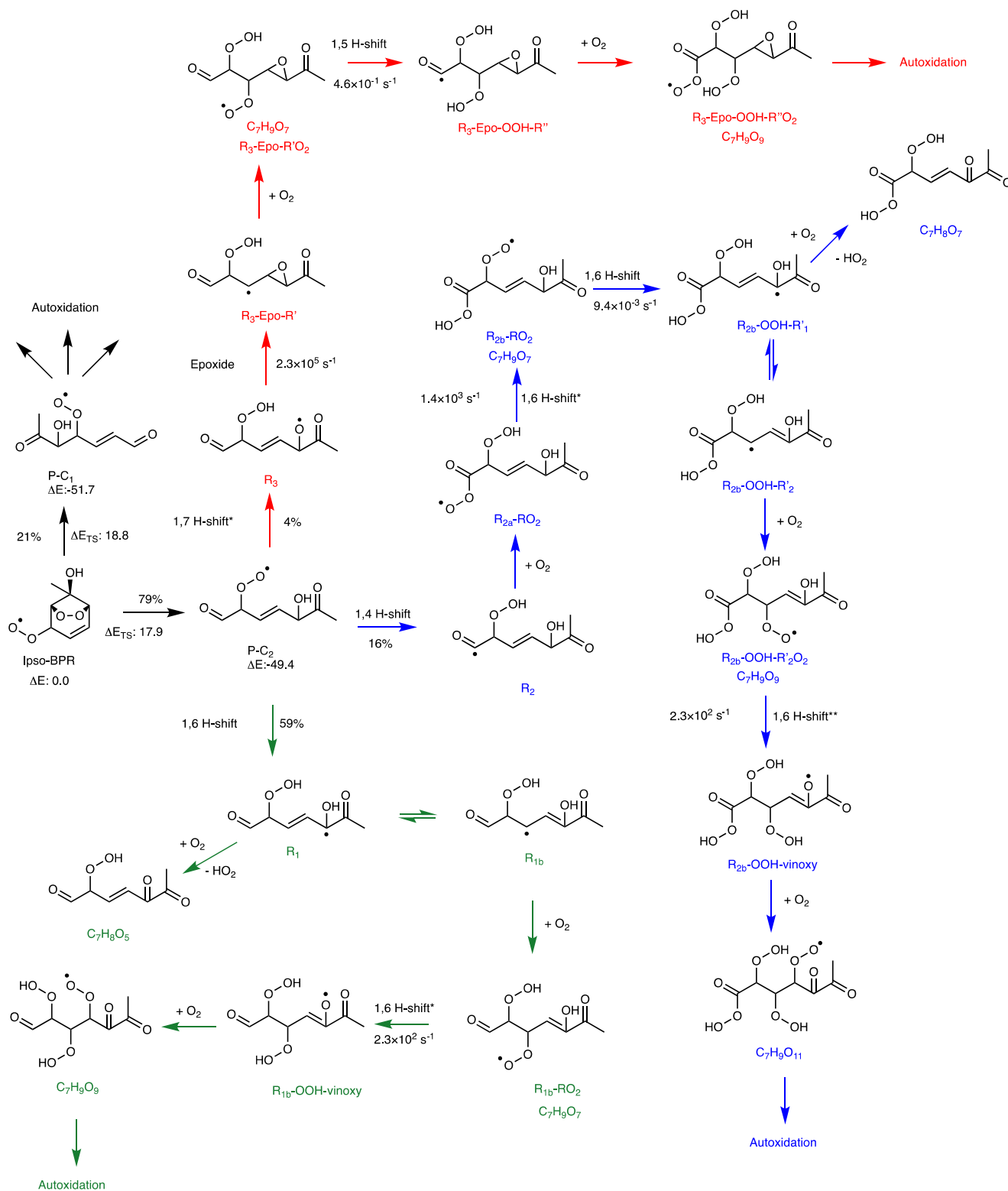
Fig. 2 | Autoxidation pathways following the molecular rearrangement reactions of i-BPR. The excess energy from the formation of P-C$_2$ allows it to access multiple autoxidation pathways. Note that P-C$_1$ and P-C$_2$ yields are 21% and 79%, respectively, and the fates of P-C$_2$ sum to 79%. *Rate coefficients calculated at the ωB97X-D/aug-cc-pVTZ level of theory, **Rate coefficient calculated at the B3LYP/6- 31+G(d) level of theory due to the large size and number of conformers for this system. The rest are calculated at the ROHF-ROCCSD(T)-F12a/VDZF12/ωB97X-D/ aug-cc-pVTZ level of theory. Method details with justifications for the different methods employed are provided in Methods.

Universal rearrangement mechanisms of aromatics

Quantum chemical calculations indicate that similar rearrangement mechanisms are key players in aromatic oxidation in general. Figure 4 shows the rate coefficients of the fastest of the two possible rearrangement mechanisms, C$_1$ and C$_2$ as shown in Fig. 1a, for select key aromatics. Like toluene, the rearrangement mechanism for the other studied aromatic molecules is fastest for i-BPRs, and for molecules, such as meta-xylene and isopropylbenzene, the rate coefficient
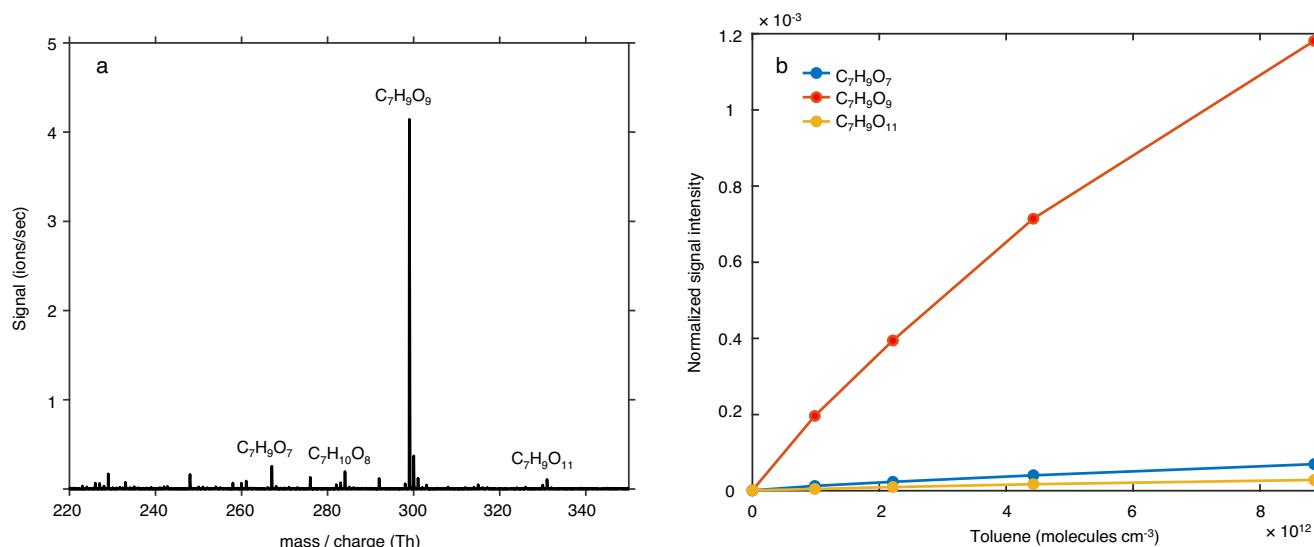
Fig. 3 | NO$_3$-CIMS experiments of the reaction of OH radicals with toluene. a Mass spectra and b normalized signals of RO$_2$ radicals as a function of toluene concentration. Reactant concentrations (unit: molecules cm^{-3}): [TME] = 1.23 × 10^{12}, [O$_3$] = 5.66 × 10^{12}, [Toluene] in Fig. 3a = 8.86 × 10^{12}. Reaction time = 3.7 s.
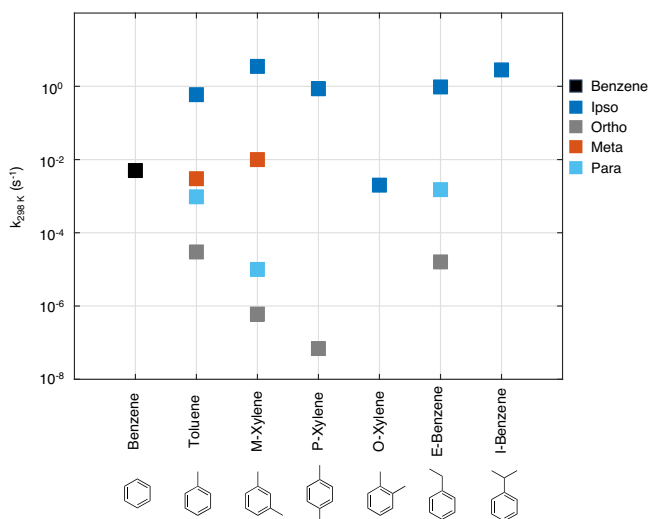

Fig. 4 | Rate coefficients of the molecular rearrangement mechanisms of select aromatics. T = 300 K. Molecules studied are benzene, toluene, meta-xylene, para-xylene, ortho-xylene, ethylbenzene and isopropylbenzene. The rate coefficients for BPRs with OH in the meta position for ethylbenzene and in the non-ipso positions for ortho-xylene and isopropylbenzene were not calculated. i-BPRs consistently have the fastest rate coefficients and are competitive under atmospheric conditions for all studied aromatic molecules.

is in excess of 1 s^{-1}. For all studied aromatic molecules, the rearrangement mechanism of i-BPRs is their dominant loss process under most atmospheric conditions, and will lead to ring broken RO$_2$s that carry significant excess energy. The subsequent autoxidation of such RO$_2$s will be different from what is currently known, as has been demonstrated here for toluene. Modeling the SOA formation from these aromatic molecules will therefore necessitate the study of their molecular rearrangement mechanisms, and the role of excess energy in their autoxidation. The findings of this study will be a crucial starting point for similar studies on the oxidation of other aromatic molecules, and also for other VOC systems containing structures that could be prone to similar rearrangements (e.g., biogenic terpenes with several cyclic structures and unsaturated sites).

Atmospheric perspective of the molecular rearrangement mechanism

Field and laboratory measurements show that the oxidation processes of aromatic molecules in general, and toluene in particular, yield SOA. However, the autoxidation mechanism leading unambiguously from toluene + OH to SOA precursors has not been reported thus far. A key challenge for establishing such a mechanism is that bicyclic peroxy radicals from toluene are sterically prevented from taking part in autoxidation. The molecular rearrangement mechanism is the dominant fate of toluene derived i-BPR, and leads directly, and in substantial yield, to hitherto undiscovered peroxy radicals P-C$_1$ and P-C$_2$ without steric constraints. These peroxy radicals have access to fast unimolecular reaction channels, and to significant excess energy, allowing them to form peroxy radicals with up to nine oxygen atoms in subsecond timescales and via multiple concurrent autoxidation channels. Our calculations also show that the molecular rearrangement mechanism is operative for bicyclic organo nitrates, and lead to organo nitrates that are completely ring broken (see Supplementary Section 7). In some cases, they can subsequently lose NO$_2$ and convert back to a radical. This could re-initiate autoxidation and provide a transport mechanism for NO$_x$, similarly as PAN do.

The molecular rearrangement mechanism reported in this work explains the rapid formation of highly oxidized organic products in one of the most important urban SOA-forming systems, toluene + OH, with potential relevance also for other atmospherically abundant aromatic molecules.

Methods

Systematic conformer sampling of the reactants, intermediates, transition states and products studied here were performed using the MMFF method in Spartan '18 (Wavefunction, Inc.) program. Radical oxygen and carbon atoms in open-shell systems were assigned as uncharged by using the keyword FFHINT On=+-0 for oxygen atoms and FFHINT Cn=+-0, respectively, where n is the atomic label of the relevant O or C atoms. For the non-transition state systems, the initial geometry optimization was carried out using the density functional theory (DFT) method B3LYP/6-31+G(d). For the ring broken systems with many tens to hundreds of possible conformers, a single-point energy calculation was carried out using the B3LYP/6-31+G(d) method, and conformers within 5 kcal/mol in relative electronic energies of the lowest-energy conformers were carried over for the geometry optimization step at the same level of theory. Conformers within 2 kcal/

mol in relative electronic energies after the geometry optimization step at B3LYP/6-31 + G(d) were re-optimized at the higher ωB97X-D/aug-cc-pVTZ level of theory. Frequencies were also calculated using this method. These computations were performed with the ultrafine grid using the Gaussian 16 program[38]. Finally, only a single lowest energy conformer for each reactant, intermediate, and product was taken for the final energy refinement step at the ROHF-ROCCSD(T)-F12a/VDZ-F12 level performed using the Molpro 2021.2 and Molpro 2022.2.2 programs[39].

For the transition states (TS), the geometries were first optimized with the bonds relevant for the TS constrained at approximate distances, followed by unconstrained transition state calculations. Both calculations were carried out at the B3LYP/6-31+G(d) level of theory. Once the TS geometry was found, the structure was taken to Spartan '18 (Wavefunction Inc.). Partial bonds were added to the TS relevant bonds and the distances constrained, and a conformer sampling step was performed using the MMFF method. If the number of conformers numbered in the tens, the single-point energy calculation at the B3LYP/6-31+G(d) was performed, and structures within 5 kcal/mol in relative electronic energies were taken for the optimization step. The constrained and unconstrained TS optimizations were repeated, this time for multiple conformers, at the B3LYP/6-31+G(d) level of theory. Transition state conformers within 2 kcal/mol in relative electronic energies were carried over for TS optimization at the ωB97X-D/aug-cc-pVTZ level of theory. For each studied TS, the energy of the lowest energy conformer was refined at the ROHF-ROCCSD(T)-F12a/VDZ-F12 (abbreviated F12) level of theory.

Rate calculations using multi-conformer transition state theory (MC-TST)

The rate-coefficients of the autoxidation steps of the ring broken peroxy radicals were calculated using the MC-TST method with Eckart tunneling[40,41]. The MC-TST expression is given by the following:

$$k = \kappa \frac{k_B T}{h} \frac{\sum_i^{\text{all TS conf.}} \exp\left(-\frac{\Delta E_i}{k_B T}\right) Q_{TS,i}}{\sum_j^{\text{all R conf.}} \exp\left(-\frac{\Delta E_j}{k_B T}\right) Q_{R,j}} \exp\left(-\frac{E_{TS} - E_R}{k_B T}\right) \quad (1)$$

Here, κ is the quantum-mechanical tunneling coefficient, T is the absolute temperature (=298.15 K), k_B is the Boltzmann's constant and h is the planck's constant. $Q_{R,j}$ and $Q_{TS,i}$ are the partition functions of the reactant and transition state conformers j and i, respectively, and ΔE_j and ΔE_i are the zero-point corrected electronic energies of the reactant and transition state conformers relative to the lowest energy conformers, respectively. E_R and E_{TS} are the zero-point corrected electronic energies of the lowest energy reactant and transition state conformers. Partition functions were calculated using DFT at the ωB97X-D/aug-cc-pVTZ level of theory, while the reaction barrier (E_{TS}-E_R) includes the F12 correction. Only those conformers that are within 2 kcal/mol of the lowest energy conformer at B3LYP/6-31+G(d) level of theory are included in the summations in the numerator and denominator, which has been reported to be adequate[40].

The Eckart approach was used to calculate the tunneling coefficient κ.[40,41] Briefly, it is based on the conformers connected to the lowest energy TS conformer by an intrinsic reaction coordinate. Barriers are calculated at the F12 level of theory, while the imaginary frequency of the TS is calculated at the ωB97X-D/aug-cc-pVTZ level of theory. Because of issues with the HF calculations converging to different possible solutions, transition state energies for H atom abstraction from -OH and -OOH groups were calculated at the ωB97X-D/aug-cc-pVTZ level of theory (without F12 corrections). Møller et al.[31] estimate that the uncertainty in the rate coefficients would increase to a factor of 100 without the F12 single-point energy corrections. This is relevant for the rate coefficients of the H-abstractions leading to intermediates R_{1b}-OOH-vinoxy, R_{2b}-RO$_2$, and R_3 in Fig. 2.

Wavefunction stability

The stabilities of the wavefunctions of the two molecular rearrangement transition states of toluene derived i-BPR were checked at the CCSD(T) stage. This was done to ensure that the lowest lying wavefunction was found. First, a CASSCF calculation was carried out with the MINAO basis set, and with the 1s and 2s orbitals of the heavy (non-H) atoms frozen. Included in the active space were, all occupied p-orbitals/electrons of H atoms, the one half-occupied orbitals for radicals, and one virtual (unoccupied) orbital to allow for rotations within the active space. This is then used as input for the RHF calculation with the larger desired basis set. These calculations were carried out with the Molpro 2022.2.2 program[39]. This is a much more robust approach for checking wavefunction stability than e.g., the standard Stable = Opt check in Gaussian. An example input file is provided in the supplementary files.

Master equation simulations

The master equation solver for multi-energy well reactions (MESMER) program[42] was used to carry out the master equation simulations. The SimpleRRKM method with Eckart tunneling was used to calculate the rate coefficients of the rearrangement reactions, C_1 and C_2, of toluene and the other aromatics derived i-BPRs. In a separate MESMER simulation, the first isomerization intermediates of the ring broken intermediates P-C_1 and P-C_2 were included to calculate the final yields. Lennard-Jones parameters for the toluene derived species: $\sigma = 5.92$ Å and $\epsilon = 410$ K, which are the values for toluene[43,44]. The exponential energy decay with an average energy transfer per collision, ΔE_{down}, was given a value of 278.89 cm^{-1}, which is based on experimental results for toluene with N$_2$ bath gas[43]. Grain size = 100 cm^{-1} and numerical precision = dd. In the simulations where the yields of the different pathways were calculated, temperature and pressure were given values of 298.15 and 760 Torr, respectively. The temperature was also varied to derive the temperature dependent rates of the two rearrangement reactions C_1 and C_2 of toluene derived i-BPR.

In the MESMER simulations, the internal modes corresponding to internal rotations were removed from the vibrational frequencies and treated as hindered rotors. This was performed by first running computations using Gaussian 16 to identify the hindered rotors, and to calculate the corresponding periodicities and barriers using the Freq = HinderedRotor keyword at the ω97X-D/aug-cc-pVTZ level of theory. For the subsequent MESMER simulation, the HinderedRotorQM1D method was used, which requires the Gaussian derived periodicities and barriers, the bonds corresponding to the hindered rotors and the removal of corresponding harmonic frequencies.

The MESMER input file used for calculating the yields of the different pathways following the rearrangement of toluene derived i-BPR is provided in the supplementary files.

Mass spectrometry experiments

Toluene and CD$_3$-toluene were mixed with OH generated by reacting ozone with tetramethylethylene in a quartz flow reactor. The products were subsequently detected by a nitrate-based chemical ionization mass spectrometer (CIMS). The reaction time was controlled by directing the toluene and CD$_3$-toluene flow through an injector tube within the flow reactor, limiting their residence time with OH from 3.7 s to 1.5 s and 0.8 s. For a given OH concentration, the concentrations of toluene and CD$_3$-toluene were varied to observe the changes in product signals. For the NO experiments, toluene/CD$_3$-toluene and OH concentrations were kept constant, while the NO concentration was varied. For the D$_2$O experiments, N$_2$ was bubbled through a D$_2$O reservoir to introduce it into the flow reactor, where it was allowed to mix with the reactants and the oxidation products. The experiments were conducted under atmospheric conditions.

Data availability

Supplemental information is available for this paper. Quantum chemical output files and plotting scripts are available online through the public research data archive Zenodo (https://doi.org/10.5281/zenodo.8214481). Source data are provided with this paper.

Code availability

The scripts used to produce the plots are provided under https://doi.org/10.5281/zenodo.8214481.

References

1. Yan, Y. et al. Global tropospheric effects of aromatic chemistry with the saprc-11 mechanism implemented in geos-chem version 9-02. *Geosci. Model Dev.* **12**, 111–130 (2019).
2. Lee, S., Chiu, M., Ho, K., Zou, S. & Wang, X. Volatile organic compounds (vocs) in urban atmosphere of hong kong. *Chemosphere* **48**, 375–382 (2002).
3. Ran, L. et al. Ozone photochemical production in urban shanghai, china: Analysis based on ground level observations. *J. Geophys. Res. Atmos.* **114**, https://doi.org/10.1029/2008JD010752 (2009).
4. Cabrera-Perez, D., Taraborrelli, D., Sander, R. & Pozzer, A. Global atmospheric budget of simple monocyclic aromatic compounds. *Atmos. Chem. Phys.* **16**, 6931–6947 (2016).
5. Ji, Y. et al. Reassessing the atmospheric oxidation mechanism of toluene. *Proc. Natl. Acad. Sci.* **114**, 8169–8174 (2017).
6. McDonald, B. C. et al. Volatile chemical products emerging as largest petrochemical source of urban organic emissions. *Science* **359**, 760–764 (2018).
7. Na, K., Kim, Y. P., Moon, I. & Moon, K.-C. Chemical composition of major voc emission sources in the seoul atmosphere. *Chemosphere* **55**, 585–594 (2004).
8. Reimann, S. & Lewis, A. C. Anthropogenic VOCs. Volatile Organic Compounds in the Atmosphere 33–81 (Oxford, Blackwell, 2007).
9. Xiao, M. et al. The driving factors of new particle formation and growth in the polluted boundary layer. *Atmos. Chem. Phys.* **21**, 14275–14291 (2021).
10. Misztal, P. K. et al. Atmospheric benzenoid emissions from plants rival those from fossil fuels. *Sci. Rep.* **5**, 1–10 (2015).
11. Colomb, A., Yassaa, N., Williams, J., Peeken, I. & Lochte, K. Screening volatile organic compounds (vocs) emissions from five marine phytoplankton species by head space gas chromatography/mass spectrometry (hs-gc/ms). *J. Environ. Monit.* **10**, 325–330 (2008).
12. Rocco, M. et al. Oceanic phytoplankton are a potentially important source of benzenoids to the remote marine atmosphere. *Commun. Earth Environ.* **2**, 1–8 (2021).
13. Wohl, C. et al. Marine biogenic emissions of benzene and toluene and their contribution to secondary organic aerosols over the polar oceans. *Sci. Adv.* **9**, eadd9031 (2023).
14. Yu, Y. et al. Polycyclic aromatic hydrocarbons not declining in arctic air despite global emission reduction. *Environ. Sci. Technol.* **53**, 2375–2382 (2019).
15. Lelieveld, J., Evans, J. S., Fnais, M., Giannadaki, D. & Pozzer, A. The contribution of outdoor air pollution sources to premature mortality on a global scale. *Nature* **525**, 367–371 (2015).
16. Duarte-Davidson, R., Courage, C., Rushton, L. & Levy, L. Benzene in the environment: an assessment of the potential risks to the health of the population. *Occup. Environ. Med.* **58**, 2–13 (2001).
17. Sarigiannis, D. A. & Gotti, A. et al. Biology-based dose-response models for health risk assessment of chemical mixtures. *Fresenius Environ. Bull.* **17**, 1439–1451 (2008).
18. Ciarrocca, M. et al. Assessment of occupational exposure to benzene, toluene and xylenes in urban and rural female workers. *Chemosphere* **87**, 813–819 (2012).
19. Bates, K. H. et al. Development and evaluation of a new compact mechanism for aromatic oxidation in atmospheric models. *Atmos. Chem. Phys.* **21**, 18351–18374 (2021).
20. Kroll, J. H. & Seinfeld, J. H. Chemistry of secondary organic aerosol: Formation and evolution of low-volatility organics in the atmosphere. *Atmos. Environ.* **42**, 3593–3624 (2008).
21. Molteni, U. et al. Formation of highly oxygenated organic molecules from aromatic compounds. *Atmos. Chem. Phys.* **18**, 1909–1921 (2018).
22. Garmash, O. et al. Multi-generation oh oxidation as a source for highly oxygenated organic molecules from aromatics. *Atmos. Chem. Phys.* **20**, 515–537 (2020).
23. Nie, W. et al. Secondary organic aerosol formed by condensing anthropogenic vapours over china's megacities. *Nat. Geosci.* **15**, 255–261 (2022).
24. Stier, P. et al. Host model uncertainties in aerosol radiative forcing estimates: results from the aerocom prescribed intercomparison study. *Atmos. Chem.Phys.* **13**, 3245–3270 (2013).
25. Schulz, M. et al. Radiative forcing by aerosols as derived from the aerocom present-day and pre-industrial simulations. *Atmos. Chem. Phys.* **6**, 5225–5246 (2006).
26. Myhre, G. et al. Radiative forcing of the direct aerosol effect from aerocom phase ii simulations. *Atmos. Chem. Phys.* **13**, 1853–1877 (2013).
27. Crounse, J. D., Nielsen, L. B., Jørgensen, S., Kjaergaard, H. G. & Wennberg, P. O. Autoxidation of organic compounds in the atmosphere. *J. Phys. Chem. Lett.* **4**, 3513–3520 (2013).
28. Iyer, S. et al. Molecular mechanism for rapid autoxidation in α-pinene ozonolysis. *Nat. Commun.* **12**, 1–6 (2021).
29. Kurten, T. et al. Computational study of hydrogen shifts and ring-opening mechanisms in α-pinene ozonolysis products. *J. Phys. Chem. A* **119**, 11366–11375 (2015).
30. D'Ambro, E. L. et al. Pathways to highly oxidized products in the δ3-carene + oh system. *Environ. Sci. Technol.* **56**, 2213–2224 (2022). PMID: 35119266.
31. Møller, K. H., Bates, K. H. & Kjaergaard, H. G. The importance of peroxy radical hydrogen-shift reactions in atmospheric isoprene oxidation. *J. Phys. Chem. A* **123**, 920–932 (2019).
32. Jenkin, M. E., Valorso, R., Aumont, B., Rickard, A. R. & Wallington, T. J. Estimation of rate coefficients and branching ratios for gas-phase reactions of oh with aromatic organic compounds for use in automated mechanism construction. *Atmos. Chem. Phys.* **18**, 9329–9349 (2018).
33. Wu, X., Huang, C., Niu, S. & Zhang, F. New theoretical insights into the reaction kinetics of toluene and hydroxyl radicals. *Phys. Chem. Chem. Phys.* **22**, 22279–22288 (2020).
34. Glowacki, D. R., Wang, L. & Pilling, M. J. Evidence of formation of bicyclic species in the early stages of atmospheric benzene oxidation. *J. Phys. Chem. A* **113**, 5385–5396 (2009).
35. Wang, S., Wu, R., Berndt, T., Ehn, M. & Wang, L. Formation of highly oxidized radicals and multifunctional products from the atmospheric oxidation of alkylbenzenes. *Environ. Sci. Technol.* **51**, 8442–8449 (2017).
36. Hyttinen, N. et al. Computational comparison of different reagent ions in the chemical ionization of oxidized multifunctional compounds. *J. Phys. Chem. A* **122**, 269–279 (2018).
37. Roldin, P. et al. Modelling non-equilibrium secondary organic aerosol formation and evaporation with the aerosol dynamics, gas- and particle-phase chemistry kinetic multilayer model adcham. *Atmos. Chem. Phys.* **14**, 7953–7993 (2014).
38. Frisch, M. et al. Gaussian 16, revision C. 01. Gaussian, Inc., Wallingford CT. 2016. http://www.gaussian.com (2016).
39. Werner, H.-J. et al. The Molpro quantum chemistry package. *J. Chem. Phys.* **152**, 144107. https://doi.org/10.1063/5.0005081 (2020).

40. Møller, K. H., Otkjær, R. V., Hyttinen, N., Kurtén, T. & Kjaergaard, H. G. Cost-effective implementation of multiconformer transition state theory for peroxy radical hydrogen shift reactions. *J. Phys. Chem. A* **120**, 10072–10087 (2016). PMID: 27992191.

41. Eckart, C. The penetration of a potential barrier by electrons. *Phys. Rev.* **35**, 1303–1309 (1930).

42. Glowacki, D. R., Liang, C.-H., Morley, C., Pilling, M. J. & Robertson, S. H. Mesmer: An open-source master equation solver for multi-energy well reactions. *J. Phys. Chem. A* **116**, 9545–9560 (2012). PMID: 22905697.

43. Hippler, H., Troe, J. & Wendelken, H. J. Collisional deactivation of vibrationally highly excited polyatomic molecules. II. Direct observations for excited toluene. *J. Chem. Phys.* **78**, 6709–6717 (1983).

44. Mourits, F. M. & Rummens, F. H. A. A critical evaluation of lennard-jones and stockmayer potential parameters and of some correlation methods. *Can. J.Chem.* **55**, 3007–3020 (1977).

Author contributions

S.I., A.S., and C.D. performed the quantum chemical calculations. A.K., S.B., S.I., O.G., and M.R. planned and conducted the flow reactor experiments. S.I. and A.K. analyzed the experimental data. L.P. and P.R. carried out the modeling of the flow reactor experiments. S.I. wrote the manuscript. S.I., A.K., S.B., P.R., O.G., P.S., T.K., and M.R. commented on and edited the manuscript.

Competing interests

The authors declare no competing interests.

Additional information

Supplementary information The online version contains supplementary material available at https://doi.org/10.1038/s41467-023-40675-2.

Correspondence and requests for materials should be addressed to Siddharth Iyer or Matti Rissanen.

Peer review information *Nature Communications* thanks Liming Wang and the other, anonymous, reviewer(s) for their contribution to the peer review of this work. A peer review file is available.

Reprints and permissions information is available at http://www.nature.com/reprints

Publisher's note Springer Nature remains neutral with regard to jurisdictional claims in published maps and institutional affiliations.